

A Boundary-Metric Evaluation Protocol for Whiteboard Stroke Segmentation Under Extreme Imbalance

Nicholas Korczynski

Rowan University

USA

korcyn28@students.rowan.edu

thelostamount@gmail.com

Abstract

The binary segmentation of whiteboard strokes is hindered by extreme class imbalance, caused by stroke pixels that constitute only 1.79% of the image on average, and in addition, the thin-stroke subset averages $1.14\% \pm 0.41\%$ in the foreground. Standard region metrics (F1, IoU) can mask thin-stroke failures because the vast majority of the background dominates the score. In contrast, adding boundary-aware metrics and a thin-subset equity analysis changes how loss functions rank and exposes hidden trade-offs. We contribute an evaluation protocol that jointly examines region metrics, boundary metrics (BF1, B-IoU), a core/thin-subset equity analysis, and per-image robustness statistics (median, IQR, worst-case) under seeded, multi-run training with non-parametric significance testing. Five losses—cross-entropy, focal, Dice, Dice+focal, and Tversky—are trained three times each on a DeepLabV3-MobileNetV3 model and evaluated on 12 held-out images split into *core* and *thin* subsets. Overlap-based losses improve F1 by more than 20 points over cross-entropy (0.663 vs. 0.438 , $p < 0.001$). In addition, the boundary metrics confirm that the gain extends to the precision of the contour. Adaptive thresholding and Sauvola binarization at native resolution achieve a higher mean F1 (0.787 for Sauvola) but with substantially worse worst-case performance ($F1 = 0.452$ vs. 0.565 for Tversky), exposing a consistency–accuracy trade-off: classical baselines lead on mean F1 while the learned model delivers higher worst-case reliability. Doubling training resolution further increases F1 by 12.7 points.

1 Introduction

Whiteboard digitization is a common step in hybrid learning and collaborative work environments: a photograph of a whiteboard is processed to extract clean stroke masks that can be imported into note-taking applications such as Microsoft OneNote. Although the task is conceptually straightforward, requiring only separation of foreground ink from a uniform background, it is surprisingly challenging in practice. Pen and marker strokes are thin, occupy only a small fraction of the image area, and vary in color, thickness, and contrast depending on the type of marker, lighting conditions, and camera angle.

Extreme class imbalance. Across the 34 original images in the dataset used in this study, the stroke pixels represent a mean of only 1.79% of the image (range 0.52–4.94%). A subset of five images containing especially thin strokes has a mean stroke fraction of just $1.14\% \pm 0.41\%$ and a mean stroke width of 11.3 ± 0.9 px, compared to $2.41\% \pm 1.11\%$ and 21.6 ± 18.1 px for the seven images with core-stroke. Under such imbalance, a trivial classifier that predicts

every pixel as background achieves $> 98\%$ pixel accuracy, making standard cross-entropy loss an unreliable training signal.

Thin-structure failures. Thin strokes are the category that is the most susceptible to failure. Downsampling during training erodes fine details, and standard losses assign equal weight to every correctly classified pixel, a regime in which the overwhelming background majority dominates the gradient. As a result, models trained with cross-entropy learn to under-predict thin strokes, achieving high pixel accuracy while missing precisely the content that matters to the end user.

Standard vs. boundary metrics. Region-based metrics such as F1 and IoU can hide boundary quality issues: a prediction may achieve moderate overlap with the ground truth, yet produce ragged or dilated contours. Boundary-aware metrics, such as boundary F1 (BF1) [5] and Boundary IoU (B-IoU) [3], restrict the evaluation to a narrow band surrounding object contours and are therefore more appropriate for quantifying the fidelity of thin structures.

Contributions. The primary contribution is not that overlap-based losses outperform cross-entropy, which is well-established, but rather a rigorous, reproducible evaluation protocol for thin-structure segmentation under extreme foreground sparsity. Specifically:

- (1) A **thin subset, boundary-aware evaluation protocol** that jointly reports region metrics (F1, IoU), boundary metrics (BF1, B-IoU), and a core/thin equity analysis, revealing performance gaps invisible to region metrics alone.
- (2) **multi-run seed training with non-parametric significance testing** (three seeds \times Wilcoxon signed-rank with Bonferroni correction), paired with per-image robustness statistics (median, IQR, worst-case), which quantify both statistical reliability and practical stability.
- (3) A **core vs. thin equity measure** that exposes how loss functions differ in their treatment of fine versus thick strokes—a diagnostic absent from prior loss-comparison studies.
- (4) A **consistency–accuracy trade-off analysis** between learned models and classical baselines (adaptive and Sauvola thresholding), demonstrating that the baselines’ higher mean F1 comes at the cost of substantially worse worst-case performance.
- (5) A **fully reproducible experimental pipeline** with publicly available code and evaluation scripts.

2 Related Work

2.1 Document and Whiteboard Segmentation

Whiteboard content extraction has been studied as a special case of document binarization. Early systems relied on color-space thresholding and connected-component analysis [7, 23]. More recently, encoder–decoder architectures such as U-Net [16] and DeepLabV3 [2] have been applied to document segmentation tasks, including text-line extraction, table detection, and handwriting isolation [6, 12]. However, most deep-learning studies target printed documents or scene text rather than the sparse, thin strokes typical of whiteboard handwriting.

2.2 Thin-Structure Segmentation

Segmentation of thin or highly elongated structures, such as blood vessels, road networks, neural fibers, and surface cracks, exhibits the same fundamental challenges as whiteboard stroke delineation, namely, pronounced class imbalance and pronounced sensitivity to boundary localization accuracy. Topology-aware losses such as cDice [19] explicitly enforce connectivity by penalizing topological breaks in tubular predictions; Skeletal-based evaluation metrics [24] complement them on the evaluation side. The curvilinear-structure literature consistently reports that standard cross-entropy under-segments thin branches and that overlap-based losses such as Dice partially mitigate the problem [14]. Recent crack and defect-detection studies [11, 15] confirm this pattern in civil-infrastructure imagery, where foreground ratios are similarly low (<5%). We do not include cDice in our ablation because our binary masks lack per-stroke instance or skeleton annotations; however, it is a natural extension (Section 7).

2.3 Loss Functions for Class Imbalance

Several loss functions have been proposed to improve segmentation under class imbalance. Dice loss [14] directly optimizes the Dice coefficient, making it insensitive to the number of true-negative pixels. Generalized Dice [20] extends Dice to multi-class settings by weighting each class inversely to its volume and reduces to standard Dice in the binary case. Focal loss [10] reduces the weight of well-classified pixels so that the gradient is dominated by hard examples near decision boundaries. The Tversky loss [17] generalizes Dice by introducing separate weights for false positives and false negatives, allowing a bias towards recall. Combinations of Dice and focal loss have been shown to outperform either component alone in medical-image segmentation [22]. Despite this body of work, systematic comparisons under the specific imbalance ratios found in whiteboard segmentation (~2% foreground) are lacking, and few studies pair loss ablations with boundary-aware metrics, per-image robustness profiling, or thin-subset equity analysis, which is the gaps this work addresses.

2.4 Modern Architectures

Transformer-based segmentation models such as SegFormer [21] and Mask2Former [4] now achieve state-of-the-art results on standard benchmarks. Their larger receptive fields may better capture global context, but they also require substantially more data and computation. We deliberately choose a lightweight CNN backbone

(MobileNetV3) to isolate the effect of the loss function from that of the architecture, and evaluating modern backbones under the same protocol is left for future work.

2.5 Boundary-Aware Evaluation

Region-based metrics such as IoU and Dice can mask boundary errors when the interior of the object is large. Boundary F1 (BF1) [5] restricts precision and recall computation to a morphological band around the contour of ground-truth. The boundary IoU [3] similarly restricts the IoU computation to a 2% diagonal band, providing a metric that is particularly sensitive to contour placement. These metrics have seen increasing adoption in instance and panoptic segmentation benchmarks but remain uncommon in document analysis.

2.6 Boundary-Aware and Topology-Aware Losses

Several losses directly optimize the boundary or topological quality. InverseForm [1] learns a differentiable approximation of the IoU boundary and has shown gains in Cityscapes and NYUDv2. cDice [19] penalizes topological breaks in tubular structures by computing Dice in skeletonized predictions. Boundary loss [9] reformulates contour-distance matching as a differentiable integral over the softmax output. These approaches are complementary to the region-based losses compared in this study; our evaluation protocol can accommodate them directly, and we identify them as a priority for future ablation (Section 7).

3 Method

3.1 Dataset

The data set consists of 34 real whiteboard photographs captured with smartphone cameras in classroom and office settings. The images have two native resolutions: 3712×2784 (30 images) and 3968×2232 (4 images). The binary masks of ground-truth were manually annotated with GIMP¹ by a single annotator; each pixel is labeled as *stroke* (255) or *background* (0).

The stroke coverage ranges from 0.52% to 4.94% of the image area (mean 1.79%, median 1.41%), confirming the extreme imbalance of the foreground and background. Table 1 summarizes the key dataset properties. A dedicated thin-stroke characterization (Section 3.5) found that the five thinnest-stroke images have a mean stroke width of 11.3 ± 0.9 px (measured by the distance transform on the skeletonized masks), compared with 21.6 ± 18.1 px for the seven thickest-stroke images.

Offline augmentation. Ten augmented variants are generated per original image, producing $34 + 340 = 374$ training samples. Augmentations are applied on two levels:

- **Weak (70%):** brightness (0.7 – 1.3), contrast (0.8 – 1.2), gamma (0.7 – 1.4), color temperature shift, Gaussian blur, Gaussian noise.
- **Strong (30%):** directional glare overlays (8 angles), shadow-band overlays (variable width and strength), combined glare+shadow. Images identified as “small-stroke” (IDs 22–37) receive a gentler augmentation profile with reduced blur and noise to preserve fine details.

¹<https://www.gimp.org/>

Table 1: Dataset summary.

Property	Value
Original images	34
Augmented images	340
Total training samples	374
Native resolutions	3712×2784, 3968×2232
Stroke coverage (mean)	1.79%
Stroke coverage (range)	0.52%–4.94%
Test images (core)	7
Test images (thin)	5

Online augmentation. During training, each sample is further augmented with random horizontal flip (50%), rotation ($\pm 10^\circ$, 50%), color jitter (brightness 0.3, contrast 0.3, saturation 0.2, hue 0.1), random brightness/contrast enhancement, Gaussian blur (30%), sharpening (30%) and random mask erosion with a kernel 2×2 (40%). The mask erosion step is specifically designed to teach the model to preserve the separation between thin adjacent strokes.

3.2 Architecture

The segmentation model is DeepLabV3 [2] with a MobileNetV3-Large [8] backbone, loaded with ImageNet-pretrained weights (weights="DEFAULT" in Torchvision). The final classification head is replaced with a 1×1 convolution mapping 256 channels to 2 classes (background, stroke), and the auxiliary classifier is removed. The model has approximately 11 M trainable parameters. All layers are fine-tuned; no parameters are frozen. DeepLabV3-MobileNetV3 was chosen deliberately for three reasons: (i) its lightweight footprint (~ 11 M parameters) matches the deployment target of a real-time scanner on consumer GPUs; (ii) the atrous spatial pyramid pooling (ASPP) module provides multi-scale context without a heavy decoder, creating a stress test for thin-stroke preservation; and (iii) fixing the architecture across all runs isolates the effect of the loss function from confounding architectural differences, which is the central variable of this study. Input images are resized (stretched, without aspect-ratio preservation) to the target training resolution and normalized with ImageNet statistics (mean = [0.485, 0.456, 0.406], std = [0.229, 0.224, 0.225]).

3.3 Loss Functions

Five loss functions are compared:

Cross-Entropy (CE). The standard pixel-wise cross-entropy loss, applied without class weighting.

Focal Loss. Following Lin et al. [10]:

$$\mathcal{L}_{\text{focal}} = -\alpha (1 - p_t)^\gamma \log p_t \quad (1)$$

with $\alpha = 0.25$ and $\gamma = 2.0$.

Dice Loss. Following Milletari et al. [14]:

$$\mathcal{L}_{\text{dice}} = 1 - \frac{2 \sum_i p_i g_i + \epsilon}{\sum_i p_i + \sum_i g_i + \epsilon} \quad (2)$$

where p_i is the predicted softmax probability for the stroke class in pixel i , g_i is the ground-truth label, and $\epsilon = 1$.

Dice + Focal. A weighted combination: $\mathcal{L} = 0.6 \mathcal{L}_{\text{dice}} + 0.4 \mathcal{L}_{\text{focal}}$.

Tversky Loss. Following Salehi et al. [17]:

$$\mathcal{L}_{\text{tversky}} = 1 - \frac{\sum_i p_i g_i + \epsilon}{\sum_i p_i g_i + \alpha \sum_i p_i (1 - g_i) + \beta \sum_i (1 - p_i) g_i + \epsilon} \quad (3)$$

with $\alpha = 0.3$, $\beta = 0.7$, biasing toward recall.

3.4 Evaluation Metrics

Region-based. F1 (Dice coefficient) and IoU (Jaccard index) measure spatial overlap between the predicted and ground-truth stroke masks:

$$\text{F1} = \frac{2 \text{TP}}{2 \text{TP} + \text{FP} + \text{FN}}, \quad \text{IoU} = \frac{\text{TP}}{\text{TP} + \text{FP} + \text{FN}}, \quad (4)$$

where TP, FP, and FN are counted at the pixel level by binarising both predicted and ground-truth masks at a fixed threshold of 127.

Boundary F1 (BF1). Contour pixels are extracted through the morphological gradient $\mathbf{C} = \delta_{3 \times 3}(\mathbf{M}) - \epsilon_{3 \times 3}(\mathbf{M})$, where δ and ϵ denote dilation and erosion with a square kernel 3×3 . A predicted contour pixel p is a *true-positive match* if any ground-truth contour pixel lies within Chebyshev distance τ , and vice versa. The tolerance is resolution-scaled:

$$\tau = \max(1, \lfloor 2 \max(H, W) / 1536 \rfloor) \text{ pixels}, \quad (5)$$

yielding $\tau = 1$ at 1024×768 and $\tau \approx 5$ at native resolution. The base tolerance of 2 pixels at the training resolution (1536×1152) corresponds to approximately 0.13% of the image width, which is comparable to the 1–2 pixel annotation uncertainty at thin-stroke boundaries; linear scaling ensures that evaluations at different resolutions remain comparable without inflating scores. Boundary precision and recall quantify the proportions of correctly matched contour pixels among the predicted and ground-truth sets, respectively, while BF1 denotes the harmonic mean of these two measures [5].

Boundary IoU (B-IoU). Following Cheng et al. [3], the IoU computation is restricted to a boundary band of width $d = 0.02 \cdot \sqrt{H^2 + W^2}$ (2% of the image diagonal). The band is efficiently computed via the Euclidean distance transform: $G_d = \{x : \text{DT}_{\bar{G}}(x) \leq d\}$, where \bar{G} is the complement of the ground-truth mask. Predicted pixels outside the band are ignored, ensuring that the metric is sensitive to contour placement rather than interior fill.

3.5 Test Splits

Twelve images are held out for testing (never seen during training or validation). They are partitioned into two groups based on a stroke-width characterization of the full dataset (computed once via the distance transform on skeletonized masks; the partition is a fixed list of image IDs, not a data-dependent threshold):

- **Core** (7 images: IDs 3, 13–17, 28): mean stroke fraction $2.41\% \pm 1.11\%$, mean stroke width 21.6 ± 18.1 px.
- **Thin** (5 images: IDs 22, 24, 27, 33, 36): mean stroke fraction $1.14\% \pm 0.41\%$, mean stroke width 11.3 ± 0.9 px.

The remaining 22 images and their 220 augmented variants form the training pool, which is split 80/20 (by alphabetical filename order) into training and validation sets. Augmented variants of test

images are automatically excluded from the training data. Specifically, any filename that begins with a test image identifier (e.g., `image_3_aug*`) is removed via prefix-based matching prior to the training procedure.

4 Experiments

4.1 Loss Ablation

Five loss functions (Section 3.3) are compared at a fixed training resolution of 1536×1152 (the higher of the two resolutions studied). Each configuration is trained three times with seeds $\{42, 123, 7\}$, resulting in $5 \times 3 = 15$ models.

Training details. All models use the AdamW optimizer [13] with learning rate 1×10^{-4} , weight decay 1×10^{-4} , cosine-annealing schedule with a linear warmup of 5-epochs, batch size 2, and a maximum of 150 epochs with early stopping (patience 15, monitoring validation loss). Training is performed on a single NVIDIA RTX 3080 (10 GB) with automatic mixed precision (AMP).

4.2 Resolution Study

To isolate the effect of input resolution on thin-structure preservation, the best-performing loss (Dice+Focal) is trained at two resolutions. Loss ablation (Section 4.1) is conducted at a fixed resolution so that loss conclusions hold under a fixed compute budget; resolution is an orthogonal lever investigated here:

- 1024×768 (the Torchvision default for DeepLabV3 demos),
- 1536×1152 (approximately $2 \times$ in each dimension).

All other hyperparameters are identical to the loss ablation. Three seeds per resolution yield $2 \times 3 = 6$ models; the 1536×1152 models overlap with the Dice+Focal runs in the loss ablation.

4.3 Classical Baseline

Three baseline methods based on non-learning are evaluated on the identical 12-image test set at the *original* spatial resolution of each image (i.e. without any resizing) to ensure a fair comparison:

- **Adaptive thresholding** using OpenCV’s `adaptiveThreshold` implementation (Gaussian method, block size 51, and offset parameter $C = 15$).
- **Otsu thresholding**, corresponding to a global binarization of the grayscale image through Otsu’s between-class variance maximization criterion.
- **Sauvola thresholding** [18], i.e. local adaptive thresholding with

$$T(x, y) = \mu(x, y) \left[1 + k(\sigma(x, y)/R - 1) \right],$$

using a window size of 51 and a parameter $k = 0.2$. Sauvola thresholding is widely adopted as a reference method for document-image binarization.

The predictions produced by deep learning models are rescaled to the original image resolution via nearest-neighbor interpolation prior to the metric computation, ensuring that all methods are evaluated at the native pixel resolution.

4.4 Metrics

Each model is evaluated in the 12 test images that have not been tested using four metrics: F1, IoU, BF1, and B-IoU (Section 3.4). The metrics are computed per image and then averaged. The results are

Table 2: Loss ablation at 1536×1152 on 12 held-out test images (mean \pm std across three seeds). Classical baselines (Table 6) are evaluated at native resolution. Dice-family losses improve F1 by more than 20 points over CE.

Loss	F1	IoU	BF1	B-IoU
CE	0.438 \pm 0.011	0.288 \pm 0.009	0.594 \pm 0.007	0.291 \pm 0.010
Focal	0.430 \pm 0.012	0.283 \pm 0.009	0.589 \pm 0.013	0.285 \pm 0.009
Dice	0.650 \pm 0.004	0.486 \pm 0.005	0.674 \pm 0.002	0.490 \pm 0.005
Dice+Focal	0.657 \pm 0.005	0.494 \pm 0.006	0.676 \pm 0.002	0.497 \pm 0.005
Tversky	0.663 \pm 0.002	0.500 \pm 0.002	0.646 \pm 0.003	0.505 \pm 0.002
Adaptive (baseline)	0.761 \pm 0.112	0.626 \pm 0.132	0.853 \pm 0.231	0.628 \pm 0.130
Sauvola (baseline)	0.787 \pm 0.112	0.660 \pm 0.131	0.860 \pm 0.229	0.663 \pm 0.131

reported as mean \pm standard deviation in three seeds. Statistical significance is assessed with the Wilcoxon signed-rank test on per-image scores (12 paired samples, averaged between seeds), with Bonferroni correction ($\alpha_{\text{corr}} = 0.05/10 = 0.005$ for 10 pairwise comparisons).

Scope of the loss comparison. We deliberately compare widely-used *region/overlap* losses (CE, Focal, Dice, Tversky, and their combinations) rather than boundary-optimized losses such as Inverse-Form [1] or cIDice [19]. Our contribution is the *boundary-metric evaluation protocol* itself, not a new loss function. Because the protocol is architecture- and loss-agnostic, it can be applied to boundary-aware losses in future work (Section 7).

5 Results

5.1 Loss Ablation

Table 2 summarizes the region and boundary metrics for all five loss functions. Dice-family losses (Dice, Dice+Focal, Tversky) uniformly outperform distribution-based losses (CE, Focal) by a wide margin: Tversky achieves an F1 of 0.663 versus 0.438 for CE – a gain of more than 20 percentage points. The difference is highly significant (Wilcoxon $p < 0.001$; Table 4). Among Dice-family losses, the differences are not statistically significant ($p > 0.15$ for all pairwise comparisons), suggesting that the primary benefit is simply switching away from a distribution-based objective rather than tuning a specific overlap-based variant.

Figure 1 visualizes these differences. CE and Focal cluster together at approximately 0.43 F1, while the three losses of the Dice-family cluster near 0.66, confirming that the choice of loss is the dominant factor in this study.

5.2 Core vs. Thin Subsets

Table 3 breaks the performance into seven *core* images and five *thin-stroke* images. All losses degrade in the thin subset, but CE and Focal suffer a larger drop (gap ≈ 0.10) than losses in the Dice-family (gap ≈ 0.06). Tversky achieves the highest thin-subset F1 (0.628) with the smallest gap, consistent with its recall-biased design.

Figure 2 presents these results graphically: the gap between the two clusters narrows substantially for overlap-based losses, with Tversky offering the most balanced core/thin trade-off.

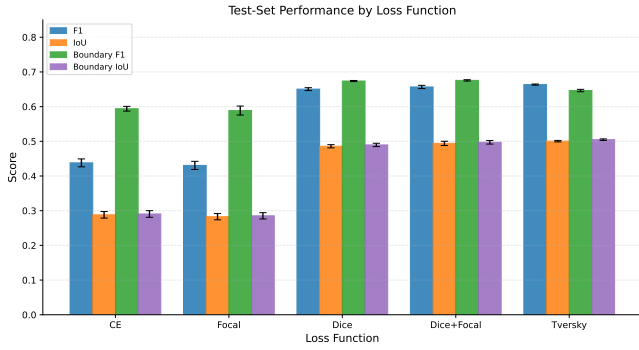


Figure 1: Region and boundary metrics per loss function. Dice-based objectives form a clearly separated, higher-performance cluster.

Table 3: Core vs. thin-subset F1. Dice-family losses halve the performance gap between subsets compared with CE/Focal, indicating better generalization to thin strokes.

Loss	Core F1	Thin F1	Gap
CE	0.480±0.010	0.378±0.013	0.102
Focal	0.476±0.010	0.367±0.015	0.109
Dice	0.674±0.006	0.618±0.003	0.056
Dice+Focal	0.685±0.009	0.618±0.003	0.067
Tversky	0.689±0.003	0.628±0.001	0.061

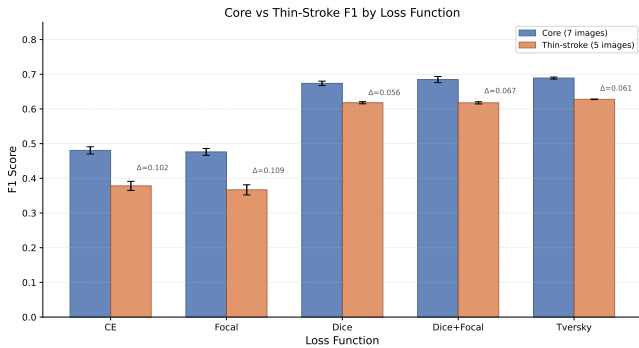


Figure 2: Core vs. thin F1 per loss. Dice-family losses narrow the gap, with Tversky showing the most balanced performance.

Figure 3 plots the absolute gap between the core and thin F1. CE and Focal exhibit gaps exceeding 0.10, while all Dice-family losses remain below 0.07.

5.3 Statistical Significance and Effect Sizes

Table 4 reports pairwise statistical tests with both mean and median effect sizes per-image. All CE/Focal vs. Dice-family comparisons are significant at $p < 0.001$ after Bonferroni correction, with a

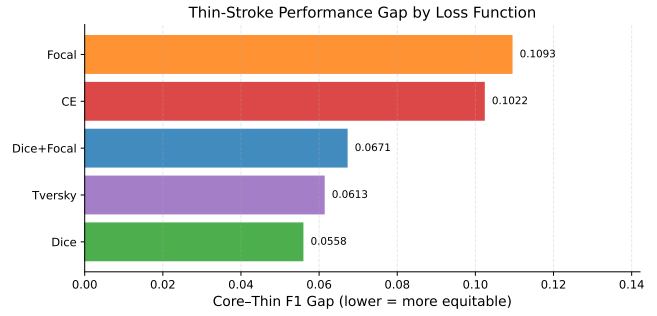


Figure 3: Core-thin F1 gap per loss. A smaller gap indicates more equitable treatment of thin strokes.

Table 4: Pairwise comparisons with mean and median per-image effect sizes (seed-averaged). * = $p < 0.001$ (Wilcoxon, Bonferroni-corrected, $\alpha = 0.005$); n.s. = not significant.**

Comparison	$\Delta F1$ (mean)	$\Delta F1$ (median)	p (Wilcoxon)	Sig.
CE vs. Focal	0.007	0.006	0.266	n.s.
CE vs. Dice	-0.213	-0.225	0.001	***
CE vs. Dice+Focal	-0.219	-0.221	0.001	***
CE vs. Tversky	-0.226	-0.237	0.001	***
Focal vs. Dice	-0.220	-0.235	0.001	***
Focal vs. Dice+Focal	-0.226	-0.239	0.001	***
Focal vs. Tversky	-0.233	-0.245	0.001	***
Dice vs. Dice+Focal	-0.006	0.000	0.850	n.s.
Dice vs. Tversky	-0.013	-0.006	0.151	n.s.
Dice+Focal vs. Tversky	-0.007	-0.009	0.380	n.s.

Table 5: Resolution ablation (Dice+Focal, three seeds). Doubling resolution yields a +13-point F1 gain and an even larger boundary-metric improvement.

Resolution	F1	IoU	BF1	B-IoU
1024×768	0.530±0.005	0.369±0.006	0.491±0.006	0.372±0.006
1536×1152	0.657±0.005	0.494±0.006	0.676±0.002	0.497±0.005

median per-image gain of +0.225 F1 points. The mean per-image improvement from CE to Dice is +0.213 ± 0.067 F1, and from CE to Tversky +0.226 ± 0.085 F1 ($p < 0.001$ in both cases), confirming that the effect is both statistically significant and practically large. Intra-Dice-family comparisons are not significant ($p > 0.15$), confirming that the dominant effect is the switch from distribution-based to overlap-based objectives, not the specific variant.

5.4 Resolution Study

Table 5 shows that increasing resolution from 1024×768 to 1536×1152 increases Dice+Focal F1 from 0.530 to 0.657 (+0.127) and BF1 from 0.491 to 0.676 (+0.185), a greater relative gain in boundary quality. Thin strokes span fewer pixels at reduced resolution, making them harder to recover.

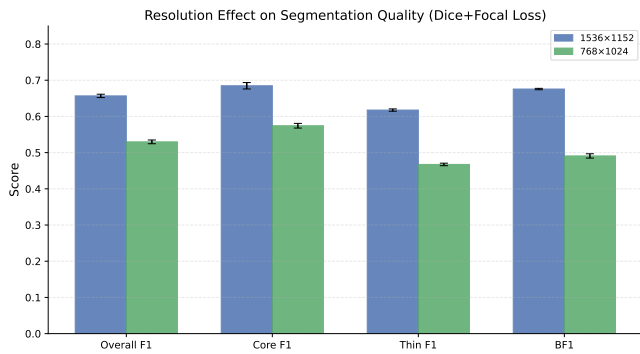


Figure 4: Resolution comparison for Dice+Focal. Boundary metrics benefit more than region metrics from higher resolution.

Table 6: Classical baselines at original resolution. Sauvola and adaptive thresholding achieve high means but show the widest per-image spread in the study; Otsu fails entirely.

Method	F1	IoU	BF1	B-IoU
Adaptive	0.761±0.112	0.626±0.132	0.853±0.231	0.628±0.130
Otsu	0.059±0.027	0.031±0.014	0.202±0.067	0.055±0.021
Sauvola	0.787±0.112	0.660±0.131	0.860±0.229	0.663±0.131

5.5 Classical Baseline

Table 6 compares three classical thresholding methods. Sauvola thresholding, a standard baseline for document-images, achieves the highest classical mean F1 (0.787), closely followed by adaptive Gaussian thresholding (0.761). However, both local methods share considerable fragility: the worst-case F1 drops to 0.452 (Sauvola) and 0.458 (adaptive) –below the Tversky minimum of 0.565. Otsu thresholding is included as a sanity baseline; its near-zero F1 (0.059) confirms that global binarization cannot cope with uneven white-board backgrounds and is not a competitive reference.

When to prefer each approach. For an application that tolerates occasional poor frames (e.g., batch archiving with manual review), Sauvola thresholding is the simplest choice: no GPU, no training, and a strong mean. For an application that requires consistent quality across all images (e.g., real-time note capture), a learned model is preferable: Tversky never drops below 0.565 F1, whereas the best classical method fails on low-contrast boards (0.452). The gap narrows further when the learned model operates at a higher resolution (Section 5.4). The mean F1 can be dominated by easy and high-contrast images; boundary metrics more directly evaluate thin-stroke fidelity, which is the primary concern in a scanner pipeline.

Figure 5 shows the three images in which the Sauvola baseline performs the worst. In image #3 – a low-contrast board with uneven lighting—Sauvola drops to F1 = 0.452, while Tversky achieves 0.796. The error overlays make the failure mode concrete: local binarization hallucinates false-positive strokes in shadow regions (blue) while simultaneously missing faint strokes (red).

Table 7: Robustness profile (per-image F1, seed-averaged). Deep models exhibit tighter IQR and higher worst-case F1 than classical baselines despite a lower mean. “Wins/12” = number of test images where the method’s F1 exceeds the best deep model’s (for classical rows) or Sauvola’s (for deep rows).

Method	Mean	Median	IQR	Min	Max	Wins/12
CE	0.438	0.413	0.157	0.230	0.667	1/12
Focal	0.430	0.398	0.183	0.223	0.684	1/12
Dice	0.650	0.653	0.054	0.542	0.791	1/12
Dice+Focal	0.657	0.649	0.072	0.528	0.789	2/12
Tversky	0.663	0.651	0.066	0.565	0.795	1/12
Sauvola	0.787	0.800	0.081	0.452	0.893	10/12
Adaptive	0.761	0.780	0.131	0.458	0.884	9/12

5.6 Robustness Analysis

Table 7 goes beyond the mean ± std and reports distributional robustness statistics for each method: median, IQR, worst-case (min), best-case (max) and paired wins against the strongest classical baseline (Sauvola).

Key observations:

- Sauvola wins on 10 of 12 images in absolute F1, but Dice-family losses beat it on the low-contrast boards where local binarization struggles most.
- Despite losing on most images, the deep models’ IQR is narrower (e.g., 0.054 for Dice vs. 0.081 for Sauvola), meaning they are more predictable.
- Tversky’s worst-case F1 (0.565) is the highest among all methods including Sauvola (0.452), making it the safest choice for failure-sensitive deployments.
- CE and Focal have IQRs far wider than Sauvola (~0.16 –0.18 vs. 0.081), indicating that under extreme imbalance, CE-family losses are not only worse on average, but also less stable.

Figure 6 reinforces this pattern: most images cluster above the parity line (Sauvola wins), but a distinct group of low-contrast boards falls well below it. In these images, the advantage of the learned model exceeds 10 F1 points.

5.7 Per-Image Analysis

Figure 7 shows per-image F1 scores across all losses. The most difficult images are those with the thinnest strokes or the lowest contrast. Dice-family losses consistently narrow the gap between easy and hard images, whereas CE and Focal exhibit bimodal behavior, nearly succeeding on some images and completely failing on others.

5.8 Training Dynamics

Figure 8 plots the training and validation loss curves for each loss function. CE and Focal converge quickly but plateau early, whereas Dice-family losses exhibit a longer, steadier descent consistent with their more informative gradients under class imbalance.

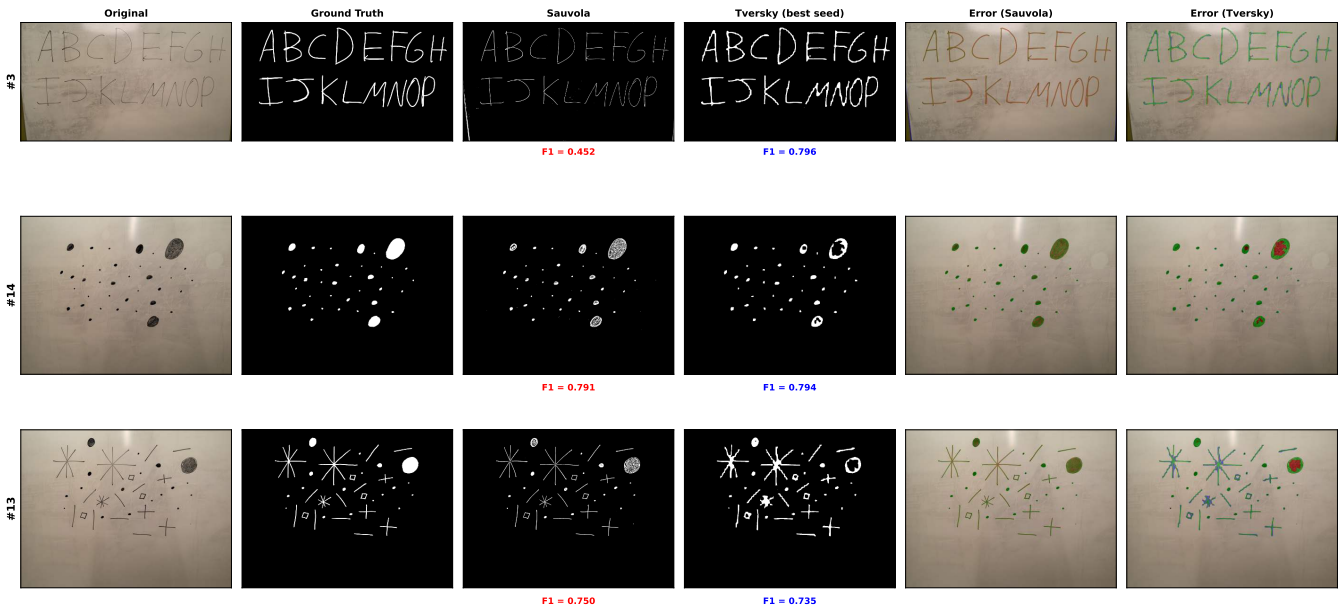


Figure 5: Classical baseline failure cases. Rows are the three images where Sauvola binarization scores lowest. Columns: original image, ground truth, Sauvola prediction, Tversky prediction, and error overlays (green = TP, red = FN, blue = FP). The deep model provides more consistent segmentation on challenging boards.

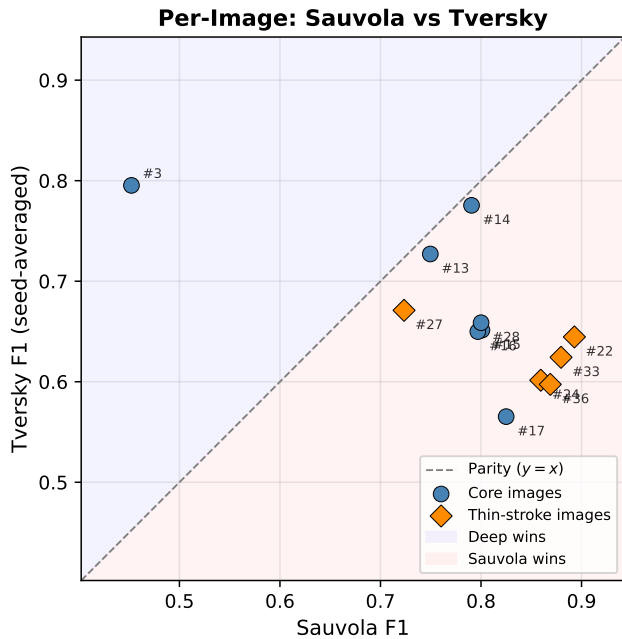


Figure 6: Per-image F1: Sauvola (x-axis) vs. Tversky (y-axis). Points below the diagonal are images where Tversky outperforms the baseline. Diamonds = thin-stroke images.

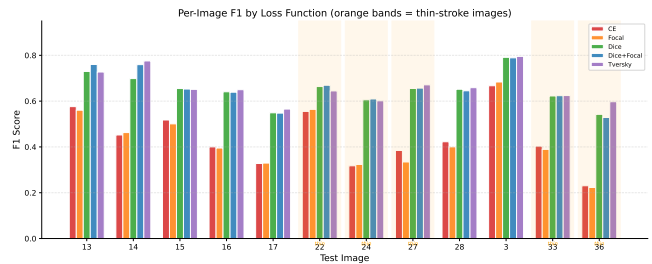


Figure 7: Per-image F1 across losses. Dice-family losses are more consistent; CE/Focal show large per-image variation.

5.9 Qualitative Results

Figure 9 presents predictions on thin-stroke images. CE/Focal produce fragmented masks that miss fine details, while Dice-family losses preserve stroke continuity. Figure 10 shows error maps for the same images, highlighting false negatives along thin strokes for CE/Focal.

Figures 11 and Figure 12 show analogous results throughout the entire test set, confirming that qualitative improvements extend beyond the thin subset.

5.10 Metric Correlations

Figure 13 presents a heatmap of all metrics across losses and seeds. BF1 and B-IoU reveal subtle differences between Dice-family variants that region metrics alone would not surface; for example,

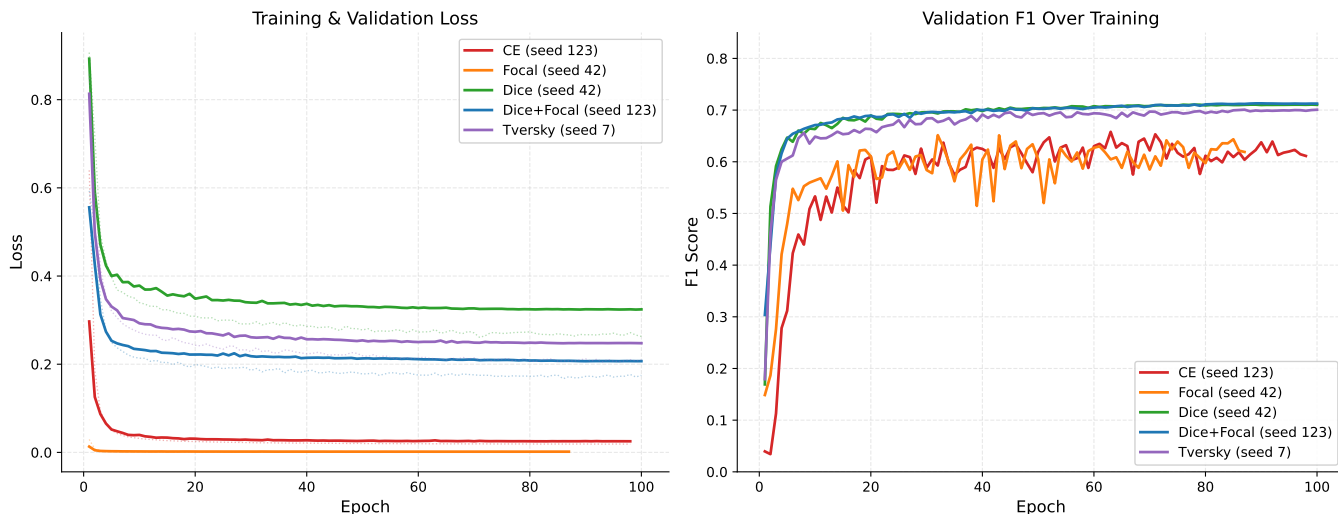


Figure 8: Training curves for each loss. Dice-family losses show a gradual, steady descent; CE/Focal converge early and plateau.

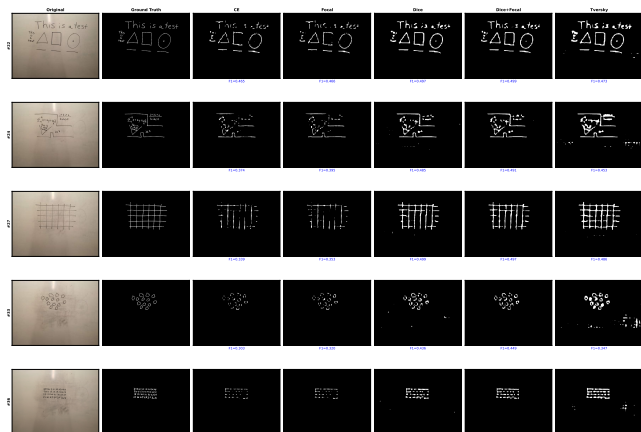


Figure 9: Qualitative predictions on thin-stroke images. Dice-family losses maintain stroke continuity where CE/Focal fragment.

Dice+Focal and Dice achieve slightly higher BF1 than Tversky despite lower F1, suggesting a precision-recall trade-off at the boundary level.

6 Discussion

6.1 Why Dice-Family Losses Dominate

The 20+ point F1 gap between CE/Focal and Dice-family losses has a straightforward explanation: under extreme class imbalance (stroke pixels $\approx 1.8\%$ of the image), CE is dominated by the easy-negative background. A model predicting “all background” achieves $>98\%$ pixel accuracy, so the per-pixel CE gradient provides almost no signal for the minority class. Focal loss re-weights by $(1 - p)^{\gamma}$, but most background pixels are already confident, leaving the effective gradient budget nearly unchanged.

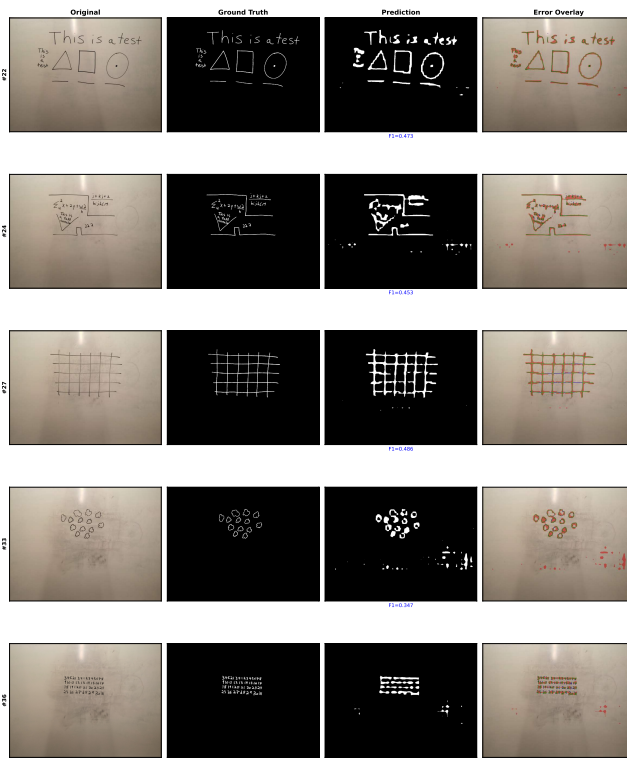


Figure 10: Error maps for thin-stroke images. Green = true positive, red = false negative, blue = false positive. CE/Focal show extensive false negatives on fine strokes.

Dice loss, by contrast, directly optimizes overlap and is invariant to the ratio of foreground to background pixels. Its gradient is proportional to the current Dice coefficient, which starts near

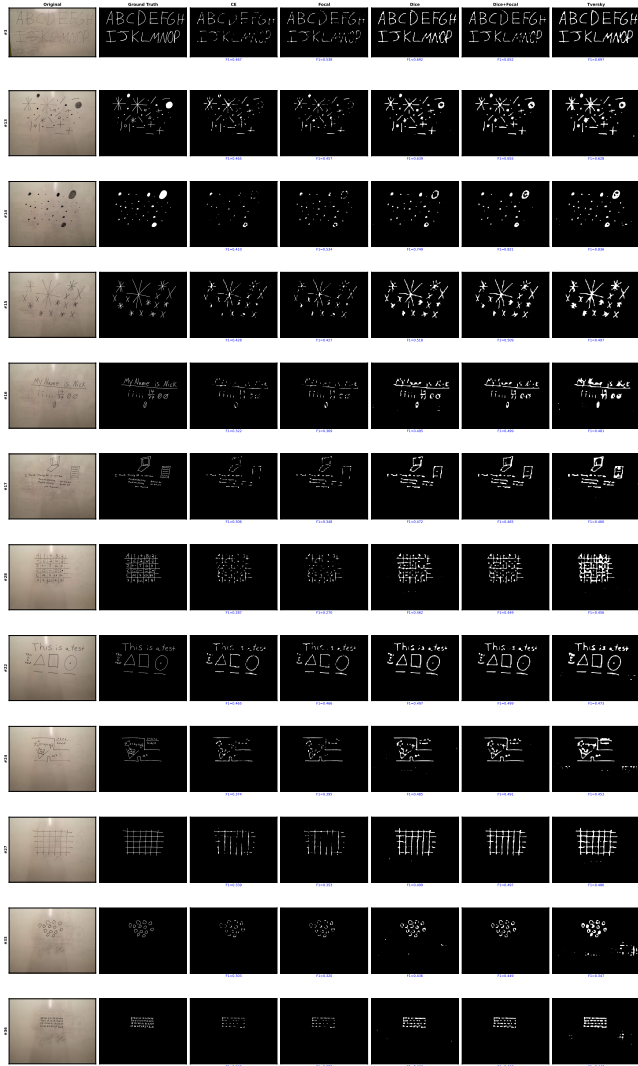


Figure 11: Qualitative predictions across the full test set. Performance trends observed on thin strokes generalise to standard images.

zero for the minority class, creating a steep learning signal precisely where it is needed. This mechanism has been theoretically analyzed [14, 22] and is consistent with our empirical results.

6.2 Tversky’s Recall Bias

The Tversky loss ($\alpha=0.3, \beta=0.7$) penalizes false negatives more than false positives, which should benefit thin strokes that are easily missed. In our results, Tversky achieves the highest F1 (0.663) and the thin-subset F1 (0.628), but the differences from Dice and Dice+Focal are not statistically significant. A possible explanation is that the recall-precision trade-off mainly shifts predictions near the existing boundary rather than recovering entirely missed strokes; this is corroborated by Tversky’s slightly lower BF1 (0.646 vs. 0.676

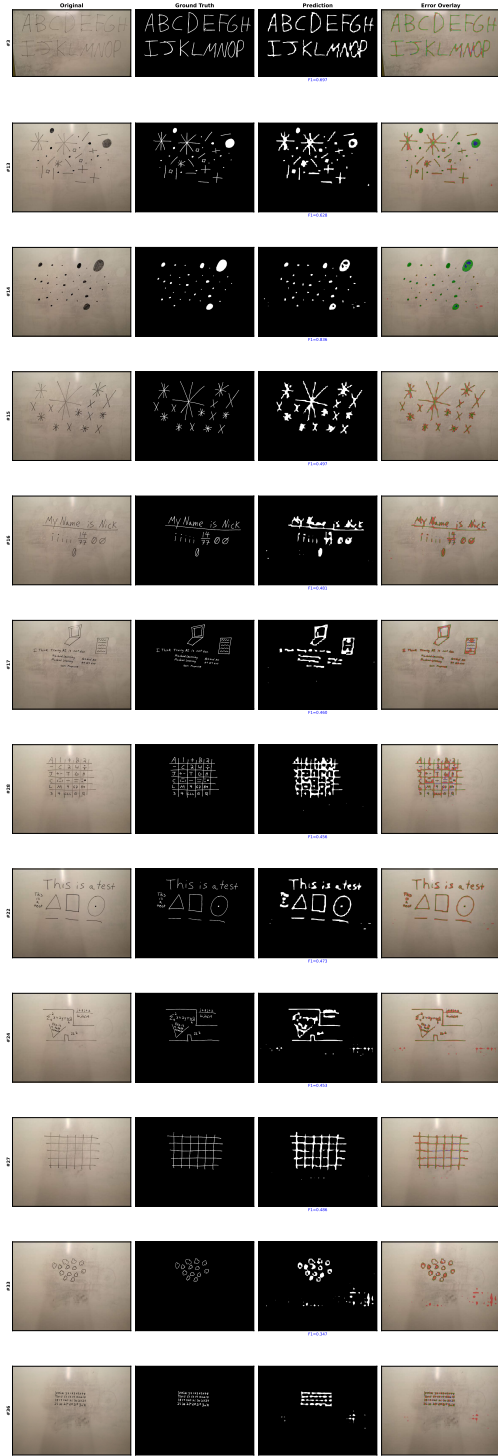


Figure 12: Error maps for the full test set. Dice-family losses consistently reduce false negatives compared with CE/Focal.

for Dice+Focal), indicating marginally less precise boundaries despite better region overlap.

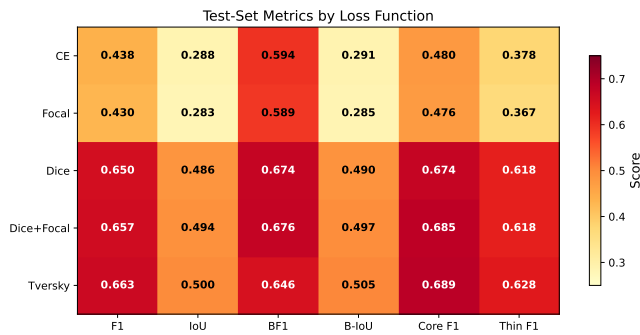


Figure 13: Metric heatmap across losses \times seeds. Boundary metrics differentiate models that region metrics rank similarly.

6.3 Boundary Metrics Reveal Hidden Differences

The region metrics (F1, IoU) rank the Dice-family losses similarly, but the boundary metrics expose a subtle trade-off. Dice+Focal achieves the highest BF1 (0.676), suggesting crisper boundaries, while Tversky leads in F1 and B-IoU. Without boundary metrics, this distinction would be invisible. We therefore endorse the recent recommendation of Cheng et al. [3] to report boundary-aware metrics alongside region-based ones, particularly for thin-structure tasks.

6.4 Consistency–Accuracy Trade-off

Sauvola binarization, the strongest classical baseline, achieves a higher mean F1 (0.787) than every deep model, but robustness analysis (Table 7) reveals the cost: an IQR of 0.081 and a worst-case F1 as low as 0.452, compared to $\text{IQR} \leq 0.072$ and worst-case ≥ 0.542 for every Dice-family model. Nevertheless, losses from the Dice-family beat Sauvola in 3 of 12 test images, specifically low-contrast boards where local binarization fails more catastrophically (Sauvola drops to $\text{F1} = 0.452$ in these images).

This pattern exposes a *consistency–accuracy trade-off*: the classical pipeline converts high-resolution information into high mean performance but provides no robustness guarantee, whereas learned models sacrifice some mean accuracy in exchange for substantially tighter per-image variance. The practical implication depends on the deployment scenario. For batch archiving of high-quality photos, the classical approach may suffice; for real-time capture under variable conditions, a learned model is preferable despite its lower ceiling.

6.5 Resolution as a Bottleneck

The resolution study confirms that the input resolution is a critical bottleneck: doubling each spatial dimension improves F1 by 13 points and BF1 by 19 points. Thin strokes that span only 1–2 pixels in 1024×768 may span 3–4 pixels in 1536×1152 , crossing the threshold at which the network can reliably segment them. Importantly, the loss-function ranking established in Section 5.1 was obtained at a constrained resolution to keep the comparison controlled, the

deployed pipeline can operate at higher resolutions where the absolute F1 is substantially higher. Resolution and loss choice are thus orthogonal levers: the former raises the performance ceiling, the latter determines which loss best exploits a given resolution. Future work should explore native-resolution or multi-scale approaches to close the remaining gap with classical baselines.

6.6 Failure Cases

Despite the improvements afforded by overlap-based losses, systematic failures remain. The most prominent failure mode occurs on extremely low-contrast strokes photographed under heavy directional glare: in these regions the stroke-to-background intensity difference falls below the network’s discrimination threshold, producing fragmented or entirely missed predictions. A secondary failure mode involves very fine strokes (< 8 px width at training resolution) that are eroded to sub-pixel width after downsampling, leaving insufficient signal for any loss function to recover. These cases are visible in the error maps (Figure 10), where red false-negative bands persist along the thinnest strokes even for the best-performing Tversky model.

6.7 Practical Implications

For production whiteboard digitization systems operating under variable lighting conditions and with mixed marker types, we recommend Dice or Tversky losses over cross-entropy whenever stroke coverage falls below approximately 5%. The consistency advantage of learned models—higher worst-case F1 and tighter IQR—is particularly valuable in real-time capture pipelines where manual review is impractical. Where computational resources permit, training at the highest feasible resolution provides a complementary and orthogonal gain.

6.8 Limitations and Scope

This study is intentionally scoped as a *controlled, deployment-constrained case study* rather than a large-scale benchmark. The protocol targets a real scanner pipeline where a lightweight model must run in real time on consumer hardware; DeepLabV3-MobileNetV3 (~11 M parameters) represents the class of models deployed, not an arbitrary legacy choice. Our goal is not state-of-the-art segmentation, but rather understanding how *loss-function choice and evaluation methodology* interact under extreme sparsity in this domain. The narrow scope of this study facilitates an exhaustive, image-wise robustness analysis and the paired statistical tests presented above. Nevertheless, several limitations should be acknowledged.

Dataset size and domain. The data set comprises 34 original images (expanded to 374 by augmentation) captured from a single whiteboard type and marker set. This scale is representative of deployment-constrained scenarios where labeled data collection is expensive; the three-seed protocol mitigates over-fitting risk and the per-image analysis (Table 7) provides fine-grained evidence. The findings should be interpreted as a controlled study of the loss-function design space under known conditions; cross-domain generalization (different whiteboard brands, markers, ambient lighting) is an empirical question for future work.

Single annotator. All masks were created by an annotator. This ensures consistent label semantics across the dataset, but inter-annotator agreement—particularly at thin-stroke boundaries where 1–2 pixel discrepancies are common—remains unmeasured.

Architecture scope. Only DeepLabV3-MobileNetV3-Large was evaluated. This choice was deliberate: a lightweight fixed architecture isolates the effect of the loss function from confounding architectural differences and matches the deployment target (a real-time scanner pipeline on consumer GPUs). Whether the observed loss-function ranking transfers to larger backbones (e.g., ResNet-101, HRNet) or modern architectures such as SegFormer [21] and Mask2Former [4] is an open question.

Resolution ceiling. Deep models were evaluated at a maximum of 1536×1152 , substantially below the native image resolution ($3712 \times 2784 / 3968 \times 2232$). Training at native resolution was computationally prohibitive for our multi-seed ablation experiments on a single 10 GB GPU. Patch-based training at native resolution therefore constitutes a natural direction for subsequent work. Importantly, the classical baseline was evaluated at *native* resolution, which favors it in region metrics. We explicitly articulate this asymmetry and acknowledge that the baseline’s advantage can diminish, or even disappear completely, if deep models are trained at higher input resolutions.

7 Conclusion

We have presented a boundary-aware evaluation protocol for binary segmentation of whiteboard strokes under extreme class imbalance (foreground $\approx 1.8\%$ of pixels). The protocol combines multi-seed training with nonparametric significance tests, per-image robustness profiling, and boundary-level metrics to provide a more complete picture of loss-function behavior than aggregate scores alone. Our key findings are as follows.

- (1) **Loss function selection is the primary determinant of performance.** Overlap-based loss functions (Dice, Dice+Focal, Tversky) increase F1 by more than 20 percentage points relative to distribution-based losses (cross-entropy, Focal), a difference that is statistically significant ($p < 0.001$, Wilcoxon signed-rank test) and associated with large effect sizes (median $\Delta F1 > 0.22$).
- (2) **Robustness is as critical as accuracy.** Dice-family loss functions yield interquartile ranges (IQR) ≤ 0.072 and worst-case F1 scores ≥ 0.542 , whereas cross-entropy exhibits an IQR of 0.157 and a worst-case score of 0.230. The strongest classical baseline (Sauvola) attains the highest mean F1 (0.787) but only a worst-case value of 0.452, highlighting a clear trade-off between consistency and peak accuracy.
- (3) **Thin strokes are disproportionately impacted.** Cross-entropy and Focal losses exhibit a core-to-thin F1 discrepancy of approximately 0.10, whereas Dice-family losses reduce this gap by half to roughly 0.06, indicating a more balanced treatment of fine-grained structures.
- (4) **Boundary-sensitive metrics are indispensable.** BF1 and B-IoU reveal boundary-level trade-offs among Dice-family variants that cannot be captured by region-based metrics alone.
- (5) **Input resolution constitutes a critical performance bottleneck.** Doubling the input resolution yields an increase of

13 points in F1 and 19 points in BF1, with even larger relative improvements observed for thin stroke regions.

7.1 Artifacts and Reproducibility

All experiments are fully reproducible. Every training run uses one of three fixed random seeds ($\{42, 123, 7\}$) with deterministic PyTorch settings (`torch.backends.cudnn.deterministic=True`) and identical data splits; all results are reported as mean \pm standard deviation across the three seeds. The public repository² contains: (i) the 34-image data set with binary masks and the augmentation pipeline, (ii) training code with the above seed and determinism configuration, and (iii) evaluation scripts that regenerate every table and figure from stored `test_set_evaluation.json` files. Pre-trained weights for all 21 models (15 loss \times 3 seed + 6 resolution \times 3 seed) in PyTorch and ONNX formats are available upon request. All experiments were conducted on a single NVIDIA RTX 3080 (10 GB).

Future work. Several directions merit further investigation: (i) training at higher spatial resolutions (or employing patch-based training pipelines at the native acquisition resolution) to reduce the performance gap relative to classical approaches, (ii) systematic evaluation of contemporary segmentation architectures, such as SegFormer [21] and Mask2Former [4], to disentangle the influence of the loss function from that of the capacity of the backbone model. (iii) conducting controlled ablation studies of *boundary-optimized* loss functions – including InverseForm [1], Boundary loss [9] and cDice [19] – under a unified experimental protocol, and (iv) expanding the data set to encompass a wider range of whiteboard brands, marker types and illumination conditions, thus enabling a more rigorous evaluation of cross-domain generalization.

References

- [1] Shashank Borse, Ying Wang, Yizhe Zhang, and Fatih Porikli. 2021. InverseForm: A Loss Function for Structured Boundary-Aware Segmentation. In *Proceedings of the IEEE/CVF Conference on Computer Vision and Pattern Recognition (CVPR)*. 5901–5911.
- [2] Liang-Chieh Chen, George Papandreou, Florian Schroff, and Hartmut Adam. 2017. Rethinking Atrous Convolution for Semantic Image Segmentation. *arXiv preprint arXiv:1706.05587* (2017).
- [3] Bowen Cheng, Ross Girshick, Piotr Dollár, Alexander C. Berg, and Alexander Kirillov. 2021. Boundary IoU: Improving Object-Centric Image Segmentation Evaluation. In *Proceedings of the IEEE/CVF Conference on Computer Vision and Pattern Recognition (CVPR)*. 15334–15342.
- [4] Bowen Cheng, Ishan Misra, Alexander G. Schwing, Alexander Kirillov, and Ross Girshick. 2022. Masked-Attention Mask Transformer for Universal Image Segmentation. In *Proceedings of the IEEE/CVF Conference on Computer Vision and Pattern Recognition (CVPR)*. 1290–1299.
- [5] Gabriela Csurka, Diane Larlus, and Florent Perronnin. 2013. What Is a Good Evaluation Measure for Semantic Segmentation? In *Proceedings of the British Machine Vision Conference (BMVC)*. BMVA Press.
- [6] Kaiming He, Georgia Gkioxari, Piotr Dollár, and Ross Girshick. 2017. Mask R-CNN. In *Proceedings of the IEEE International Conference on Computer Vision (ICCV)*. 2961–2969.
- [7] Li-Wei He and Zhengyou Zhang. 2005. Real-Time Whiteboard Capture and Processing Using a Video Camera for Remote Collaboration. In *IEEE Transactions on Multimedia*, Vol. 7. IEEE, 69–79.
- [8] Andrew Howard, Mark Sandler, Bo Chen, Weijun Wang, Liang-Chieh Chen, Mingxing Tan, Grace Chu, Vijay Vasudevan, Yukun Zhu, Ruoming Pang, Quoc V. Le, and Hartmut Adam. 2019. Searching for MobileNetV3. In *Proceedings of the IEEE/CVF International Conference on Computer Vision (ICCV)*. 1314–1324.

²<https://github.com/TheRealManual/OneNote-Whitebord-Scanner-Training>

- [9] Hoel Kervadec, Jihene Bouchtiba, Christian Desrosiers, Éric Granger, Jose de Guise, and Ismail Ben Ayed. 2019. Boundary Loss for Highly Unbalanced Segmentation. In *International Conference on Medical Imaging with Deep Learning (MIDL)*. PMLR, 285–296.
- [10] Tsung-Yi Lin, Priya Goyal, Ross Girshick, Kaiming He, and Piotr Dollár. 2017. Focal Loss for Dense Object Detection. In *Proceedings of the IEEE International Conference on Computer Vision (ICCV)*. 2980–2988.
- [11] Yingchao Liu, Jiaxing Yao, Xiaohu Lu, Renping Xie, and Li Li. 2019. DeepCrack: A Deep Hierarchical Feature Learning Architecture for Crack Segmentation. *Neurocomputing* 338 (2019), 139–153.
- [12] Jonathan Long, Evan Shelhamer, and Trevor Darrell. 2015. Fully Convolutional Networks for Semantic Segmentation. In *Proceedings of the IEEE Conference on Computer Vision and Pattern Recognition (CVPR)*. 3431–3440.
- [13] Ilya Loshchilov and Frank Hutter. 2019. Decoupled Weight Decay Regularization. In *International Conference on Learning Representations (ICLR)*.
- [14] Fausto Milletari, Nassir Navab, and Seyed-Ahmad Ahmadi. 2016. V-Net: Fully Convolutional Neural Networks for Volumetric Medical Image Segmentation. In *International Conference on 3D Vision (3DV)*. IEEE, 565–571.
- [15] Bryan G. Pantoja-Rosero, Doruk Oner, Mateusz Kozinski, Pascal Fua, and Katrin Beyer. 2022. TOPO-Loss for Continuity-Preserving Crack Detection Using Deep Learning. *Construction and Building Materials* 344 (2022), 128264.
- [16] Olaf Ronneberger, Philipp Fischer, and Thomas Brox. 2015. U-Net: Convolutional Networks for Biomedical Image Segmentation. In *Medical Image Computing and Computer-Assisted Intervention (MICCAI)*. Springer, 234–241.
- [17] Seyed Sadegh Mohseni Salehi, Deniz Erdogmus, and Ali Gholipour. 2017. Tversky Loss Function for Image Segmentation Using 3D Fully Convolutional Deep Networks. In *International Workshop on Machine Learning in Medical Imaging (MLMI)*. Springer, 379–387.
- [18] Jaakko Sauvola and Matti Pietikäinen. 2000. Adaptive Document Image Binarization. *Pattern Recognition* 33, 2 (2000), 225–236.
- [19] Suprosanna Shit, Johannes C. Paetzold, Anjany Sekuboyina, Ivan Ezhov, Alexander Unber, Andrey Zhylka, Josien P. W. Pluim, Ulrich Bauer, and Bjoern H. Menze. 2021. cDice—A Novel Topology-Preserving Loss Function for Tubular Structure Segmentation. In *Proceedings of the IEEE/CVF Conference on Computer Vision and Pattern Recognition (CVPR)*. 16560–16569.
- [20] Carole H. Sudre, Wenqi Li, Tom Vercauteren, Sébastien Ourselin, and M. Jorge Cardoso. 2017. Generalised Dice Overlap as a Deep Learning Loss Function for Highly Unbalanced Segmentations. In *Deep Learning in Medical Image Analysis and Multimodal Learning for Clinical Decision Support (DLMIA/ML-CDS)*. Springer, 240–248.
- [21] Enze Xie, Wenhai Wang, Zhiding Yu, Anima Anandkumar, Jose M. Alvarez, and Ping Luo. 2021. SegFormer: Simple and Efficient Design for Semantic Segmentation with Transformers. In *Advances in Neural Information Processing Systems (NeurIPS)*, Vol. 34. 12077–12090.
- [22] Michael Yeung, Evis Sala, Carola-Bibiane Schönlieb, and Leonardo Rundo. 2022. Unified Focal Loss: Generalising Dice and Cross Entropy-Based Losses to Handle Class Imbalanced Medical Image Segmentation. *Computerized Medical Imaging and Graphics* 95 (2022), 102026.
- [23] Fang Yin, Qiu Chen, and Jie Sun. 2007. Whiteboard Reading from Projection-Camera System. In *International Conference on Document Analysis and Recognition (ICDAR)*. IEEE, 1198–1202.
- [24] Sixiao Zheng, Jiachen Lu, Hengshuang Zhao, Xiatian Zhu, Zekun Luo, Yabiao Wang, Yanwei Fu, Jianfeng Feng, Tao Xiang, Philip H. S. Torr, and Li Zhang. 2021. Rethinking Semantic Segmentation from a Sequence-to-Sequence Perspective with Transformers. In *Proceedings of the IEEE/CVF Conference on Computer Vision and Pattern Recognition (CVPR)*. 6881–6890.